



# Monte Carlo Simulation of Heat-Affected Zone Microstructure in Laser-Beam-Welded Nickel Sheet

*Reasonable agreement was obtained between experimental results and simulated grain growth in the heat-affected zone*

BY M.-Y. LI AND E. KANNATEY-ASIBU, JR.

**ABSTRACT.** The heat-affected zone grain structure that evolves during welding of a nickel 270 sheet was simulated using Monte Carlo techniques. A matrix consisting of 200 x 200 sites with 100 possible grain orientations was used for the simulation, and the temperature histories measured during welding were used as inputs to perform the simulation. The unit length of each site is 10  $\mu\text{m}$ , with the overall simulation region being 2 x 2 mm. The simulation pertained to microstructure in the vertical plane where the temperatures were measured, i.e., along the welding direction.

The grain size throughout the heat-affected zone, as obtained by simulation, showed reasonable agreement with the experimental results obtained from metallographic examination. The differences in average grain size measurements obtained experimentally and by simulation were 12.9% and 5.8% at locations 1.26 mm and 1.70 mm below the weld centerline, respectively. The advantages of using this simulation method are to predict grain size distribution in the HAZ. The results could subsequently be used for predicting other mechanical properties of a weldment.

## Introduction

In their classic work, Burke and Turnbull proposed a parabolic grain growth

M.-Y. LI, Ph.D., is with TWB Co., Monroe, Mich. E. KANNATEY-ASIBU, JR., is a Professor, Department of Mechanical Engineering, The University of Michigan, Ann Arbor, Mich.

relationship, hypothesizing that grain growth is the result of grain boundary migration (Ref. 1), and assuming surface tension of the boundaries is the driving force for grain growth after recrystallization. A similar relationship was subsequently developed by Feltham (Ref. 2), Hillert (Ref. 3), and Saetre, et al. (Ref. 4). This parabolic relationship has been verified experimentally in nickel (Ref. 5), copper (Ref. 6), and alpha brasses (Ref. 7).

The properties of a material are not only affected by the size of its grains but also by the geometry (shape and orientation) of the grains (Ref. 8). To predict grain geometry and grain size, use of topological simulation methods is necessary. A Monte Carlo-based grain growth simulation technique was developed by Srolovitz, Anderson, and their coworkers (Refs. 9, 10). Their algorithm provides a nondimensional simulation applicable only to isothermal grain growth. Gao and Thompson developed a real-time,

temperature-dependent technique using isothermal matrices to predict grain size at different temperatures (Ref. 11). Defining a probability of  $MCS(x)/MCS_{max}$  for grain growth simulation and using the Rosenthal equation for calculating temperature cycles, Radhakrishnan and Zacharia predicted the grain growth of the HAZ of Cr-Mo-V steel (Ref. 12).

In this research, a matrix containing sites with a distributed temperature is considered necessary for predicting the HAZ microstructure. Toward this end, a dimensionalized simulation method has recently been developed (Ref. 13) to simulate grain growth in the heat-affected zone. This simulation requires temperature histories at various locations of the heat-affected zone as input. The unit length of the simulation matrix is determined by the region of interest, being 10  $\mu\text{m}$  for a 2 x 2 mm region.

Measurement of temperature histories during laser beam welding is a difficult process. Moon and Metzbower imbedded thermocouples in a laser-beam-welded steel plate and measured the peak temperatures in the molten metal (Refs. 14 and 15). In this research, temperature histories at different distances from the root of a weld centerline were measured by imbedding thermocouples into the specimen to different depths from the root side.

## Background Theory

Grain growth is the process by which

### KEY WORDS

HAZ  
Heat-Affected Zone  
Monte Carlo  
Grain Growth  
Nickel Sheet  
Ni 270  
Temperature History  
Simulation

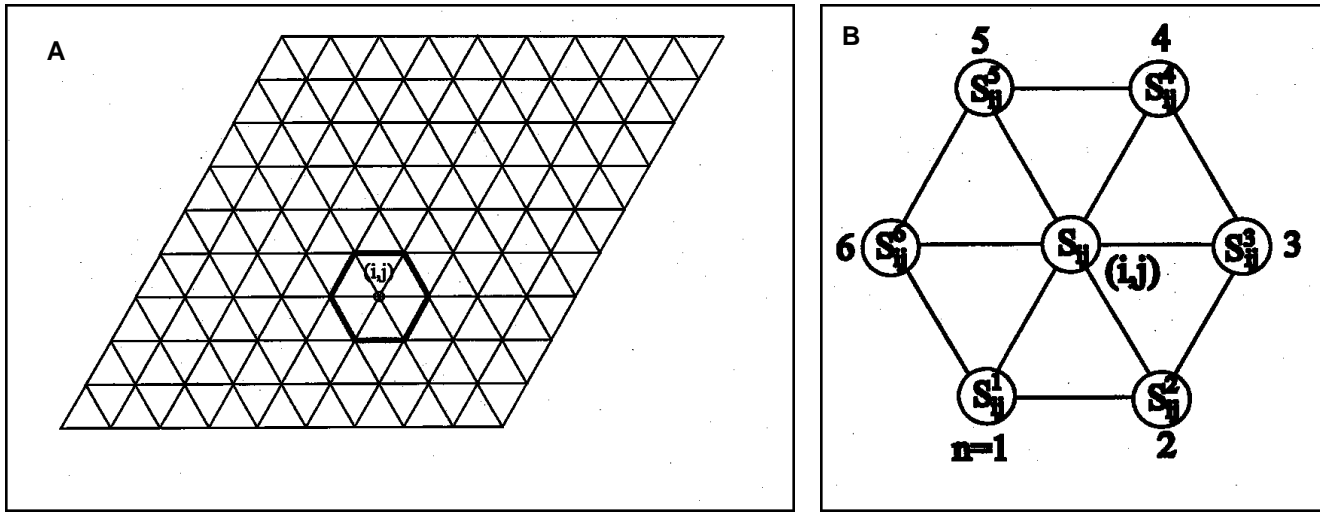


Fig. 1 — A — A triangular lattice; B — an element at location (i,j) with six nearest neighbors, where  $S_{ij}$  is the orientation of site (i,j) and  $S^n_{ij}$  is the orientation of its n-th neighbor.

the average size of crystals in a system increases. The driving force for grain growth is the decrease of free energy in the system and is associated with reorientation of the atoms. Therefore, the average grain size of a microstructure increases by some of the grains consuming other grains, thereby reducing the number of grains in a specific aggregate. Two grain-growth mechanisms have been widely studied: normal and abnormal grain growth. Normal grain growth has a relatively narrow range of grain sizes and shapes. However, unlike normal grain growth, abnormal grain growth usually has a wide range of grain sizes and shapes. Abnormal grain growth, sometimes called secondary recrystallization, is usually caused by heterogeneous system energy distribution or the existence of impurities.

Most normal grain growth theories assume negligible heat transfer, so the process may be considered to be isothermal. Assuming solid-state transformation in a pure substance starts from a stable spherical nucleus in which grain boundary energy is isotropic, and neglecting surface energy or capillary effects, and finally, assuming that growth occurs continuously on the grain boundary where the atoms can successfully attach themselves, the expression for normal grain growth can be written as (Ref. 1)

$$G = \lambda v \exp \frac{-E_A}{RT} \left( 1 - \exp \frac{-E}{RT} \right) \quad (1)$$

where  $G$  is the growth rate,  $\lambda$  is the atomic spacing,  $v$  is the jump frequency of the system,  $E_A$  is the energy barrier for grain growth per mole atom,  $E$  is the average free energy change per mole atom during grain growth,  $T$  is the absolute tempera-

ture, and  $R$  is the universal gas constant. Assuming the energy change  $E \ll RT$  during isothermal grain growth at high enough temperatures, the last term of Equation 1,

$$1 - \exp \frac{-E}{RT}$$

may be approximated as  $\frac{E}{RT}$ ,

using exponential series and neglecting higher order terms. Equation 1 then reduces to the form

$$G = \frac{\lambda v}{RT} E \exp \frac{-E_A}{RT} \quad (2)$$

Now  $E = \frac{C_0 \gamma V}{RT}$  and  $G = \frac{dr}{dt}$  where  $C_0$  is a constant,  $\gamma$  is the grain boundary interfacial energy,  $V$  is the volume per mole atom, and  $r$  is the grain boundary radius (Ref. 1). Equation 2 then becomes

$$\frac{dr}{dt} = \frac{C_0 \lambda v \gamma V}{RT r} \exp \frac{-E_A}{RT} \quad (3)$$

Equation 3 can be rewritten as

$$\frac{dr}{dt} = \frac{M}{r} \quad (4)$$

where  $M$  is defined as the atomic mobility and is constant for an isothermal system.

$$M = \frac{C_0 \lambda v \gamma V}{RT} \exp \frac{-E_A}{RT} \quad (5)$$

For isothermal grain growth, Equation 4 can be integrated to give

$$r^2 - r_0^2 = 2M t \quad (6)$$

where  $r_0$  is the initial average grain radius.

## Grain Growth Simulation

### Dimensionless Simulation

The dimensionless Monte Carlo grain growth simulation employs a two-dimensional triangular lattice in which each site has six nearest neighbors at identical distances. Each site is initially assigned a random orientation  $S_{ij}$ . A grain is defined by a group of contiguous sites with the same grain orientation  $S_{ij}$ . Grain boundaries are assumed to exist between grains with different orientations. The simulation starts by selecting a random orientation  $S_{ij}$ , from 1 to  $Q$ , where  $Q$  is the number of possible orientations for a randomly selected site (i, j). In their research, Anderson, et al. (Ref. 10), found that for  $Q = 30$ , the grain size distribution from Monte Carlo simulation approaches a limit form. Therefore,  $Q = 100$  is used in this research.  $N$  reorientation trials are referred to as a Monte Carlo step (MCS), where  $N$  is the number of sites in the matrix.

As in the case of Srolovitz, et al. (Ref. 9), the grain boundary energy  $E_{ij}$  is the driving force for the motion of a grain boundary and is defined as

$$E_{ij} = -J \sum_{n=1}^m (\delta_{s_{ij} s_{ij}^n} - 1) \quad (7)$$

where  $\delta_{s_{ij} s_{ij}^n}$  is the Kronecker delta and  $m$  is the number of nearest neighbor sites,  $s_{ij}^n$ .  $m = 6$  for a triangular lattice — Fig. 1.  $J$  is the system energy contribution from two nearest neighbor sites with different orientations, and it is a positive constant. The value of  $J$  is not necessary for the dimensionalized simulation since the probability  $P_2$  (to be defined later)

only considers its sense.  $E_{ij}$  is positive when the two nearest neighbor sites are of unlike orientation and zero otherwise. The sum is taken over all nearest neighbor sites. The energy change associated with a reorientation is calculated as

$$E_{ij} = E_{ij,new} - E_{ij,old} \quad (8)$$

where  $E_{ij,new}$  is the energy of site (i,j) after reorientation and  $E_{ij,old}$  is the energy of site (i,j) before reorientation.

A probability P was introduced by Anderson, et al. (Ref. 10), and defined as

$$P = \begin{cases} 1 & \text{if } E_{ij} \leq 0 \\ \exp\left(-\frac{E_{ij}}{RT}\right) & \text{if } E_{ij} > 0 \end{cases} \quad (9)$$

A positive  $E_{ij}$  indicates the system energy change increases after reorientation. On the other hand, a negative  $E_{ij}$  indicates a decrease of system energy after reorientation. Thus, this probability can be modified and defined as probability  $P_2$

$$P_2 = \begin{cases} 1 & \text{if } E_{ij} \leq 0 \\ 0 & \text{if } E_{ij} > 0 \end{cases} \quad (10)$$

The probability  $P_2$  forces the simulation to accept only those reorientation trials associated with decreasing total system energy. A reorientation trial is accepted if this probability criterion is satisfied. A flow chart of the simulation procedure is shown in Fig. 2.

**Dimensionalized Simulation**

**Simulation Algorithm**

The isothermal simulation algorithm developed by Anderson and coworkers (Ref. 10) was modified to incorporate temperature variation by using the original Burke and Turnbull grain growth theory. Figure 3 shows the modified procedure. Unlike the dimensionless simulation, a new probability term  $P_1$  was introduced to incorporate absolute temperature into the new simulation. Considering Equation 2,  $P_1$  is determined by

$$P_1 = \exp\left(-\frac{E_A}{RT}\right) \quad (11)$$

where  $E_A$  is the activation energy for grain growth.  $P_1$  represents the probability that an atom will overcome the energy barrier of grain growth  $E_A$ . A simulation trial satisfying the  $P_1$  criterion implies that the atom overcomes the energy barrier and has a potential to change its orientation. As mentioned in the preceding section, another probability term  $P_2$  is considered when an atom attempts to

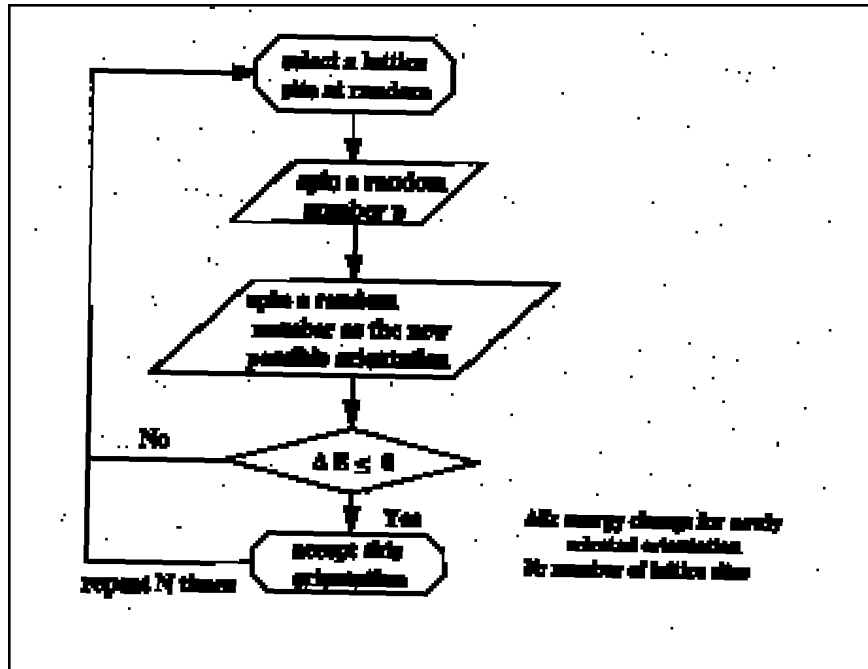


Fig. 2 — Procedure of dimensionless Monte Carlo normal grain growth simulation.

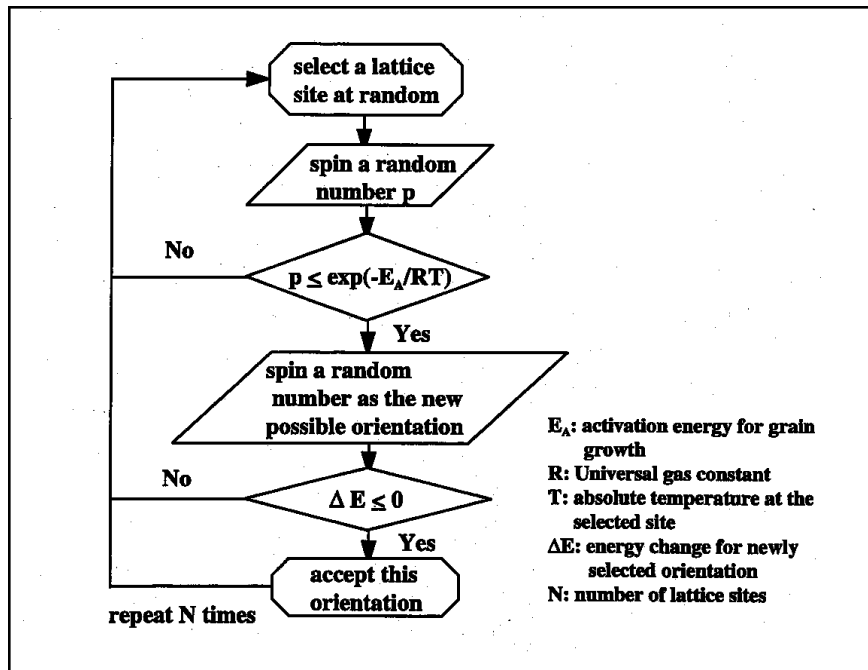


Fig. 3 — Procedure of dimensionalized Monte Carlo normal grain growth simulation.

change its location relative to its neighboring atoms, by which the grain orientation is changed, after satisfying the  $P_1$  criterion. The new orientation is accepted when  $P_2$  is also satisfied, i.e., the system total energy is lowered. Therefore, a reorientation trial is successful when both criteria  $P_1$  and  $P_2$  are satisfied.

**Grain Growth Exponent n and Coefficient  $K_s$  for Simulation**

In addition to temperature, two other parameters are required for dimensionalization, viz. temporal and spatial parameters. Isothermal simulations at various

**Table 1 — Parameters Used in the Simulation**

Symbol	Units	Value	Description
$\mu$	$\mu\text{m}$	10	Unit length of the simulation matrix
$K_0$	$\text{m}^2/\text{s}$ (Ref. 16)	$1.36 \times 10^{-3}$	Grain growth coefficient of nickel
$E_A$	$\text{kcal}/(\text{mol}^\circ\text{K})$ (Ref. 16)	27.5	Normal grain growth activation energy of nickel
$K_s$	$^2/\text{MCS}$	0.0151	Grain growth coefficient for simulation
$t_s$	s	$1.11 \times 10^{-9}$	The time each MCS represents.
$Q$	NA	100	Number of possible orientations

**Table 2 — Activation Energies for the Grain Boundary Self-Diffusion of Nickel**

Misfit Angle Energy (degrees)	Activation (kcal/g mole)
20	27.1
30	25.6
40	25.3
45	25.7
50	24.6
60	26.2
70	27.3
80	33.7

temperatures were therefore undertaken to determine the grain growth parameters of the following equation:

$$D_s^n - D_{s0}^n = K_s P_1 t_s \quad (12)$$

where  $D_s$  and  $D_{s0}$  are the final and initial average grain size of the simulation, respectively,  $n$  is the grain growth exponent [ $n = 2$  for nickel (Ref. 16)],  $K_s$  is the grain growth coefficient of the Monte Carlo simulation with units  $^2/\text{MCS}$ ,  $\mu$  is the unit length of the simulation matrix,  $t_s$  is the number of simulation steps, and  $P_1$  is the probability term introduced in Equation 11. Figure 4 shows the results of isothermal simulations with  $P_1$  equal to 1.0 and 0.1. The matrix is a triangular lattice with  $200 \times 200$  elements and 100 possible orientations randomly distributed at the beginning of the simulation. From these simulations, the grain growth exponent for simulation was determined as discussed in the following paragraphs.

From Equations 6 and 12, the mobility  $M_s$  can be assumed to be given by

$$M_s = K_s P_1 \quad (13)$$

$M_s$  is then given by the slope of the plot

of  $D_s^n - D_{s0}^n$  against  $t_s$ . Taking the natural logarithm on both sides of Equation 13 gives

$$\ln(M_s) = \ln(K_s) + \ln(P_1) \quad (14)$$

Thus, the slope of a  $\ln(M_s)$  vs.  $\ln(P_1)$  plot should be unity, and the intercept on the  $\ln(M_s)$  axis,  $\ln(K_s)$ .

The slopes of the lines that best fit the data points in Fig. 4A and B are  $1.58 \times 10^{-2}$  and  $1.57 \times 10^{-3}$ , respectively. Additional results were obtained for simulations with probabilities from  $10^{-2}$  to  $10^{-7}$ . Figure 5 shows the best-fit line for a plot of  $M_s$  vs.  $P_1$  on a natural log-log graph for  $n = 2.0$ .

The growth coefficient  $K_s$  is determined by Equation 14, i.e., the intercept of the straight line and the  $\ln(M_s)$  axis in Fig. 5. The equation of the line is given as

$$\ln(M_s) = 0.924 \ln(P_1) - 4.195 \quad (15)$$

Therefore,  $\ln(K_s) = -4.195$  and the value of  $K_s$  is 0.0151 (units:  $^2/\text{MCS}$ ) for simulations with 100 possible orientations, where  $\mu$  is the unit length of the simulation matrix.

**Temporal and Spatial Parameters**

Experimental results have shown the grain growth exponent  $n$  for nickel is 2 (Ref. 16). To incorporate the experimental data into the simulations, the grain growth exponent  $n = 2$  was employed. That gives the units of the experimental grain growth coefficient,  $K_0$ , as  $\text{m}^2/\text{s}$  and those of the simulations as  $^2/\text{MCS}$ , where  $\mu$  is the unit length of the matrix and MCS is the Monte Carlo Step or the simulation step.  $t_s$  is determined by the region of interest and the size of the matrix. Since  $K_s$  and  $K_0$  are equivalent, we have

$$K_s \frac{\delta^2}{\text{MCS}} = K_0 \frac{\text{m}^2}{s} \quad (16a)$$

or

$$\text{MCS} = \frac{K_s}{K_0} \frac{\delta^2}{\text{m}^2} s \quad (16b)$$

Equation 16b determines the amount of time that an MCS represents when the length of  $\mu$  is set. For example, for a  $2 \times$

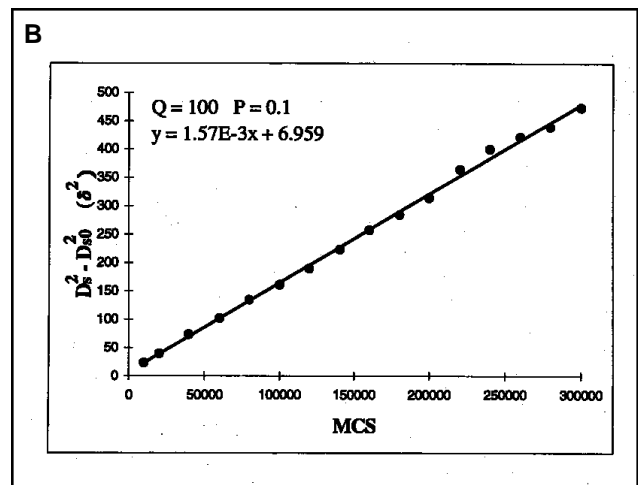
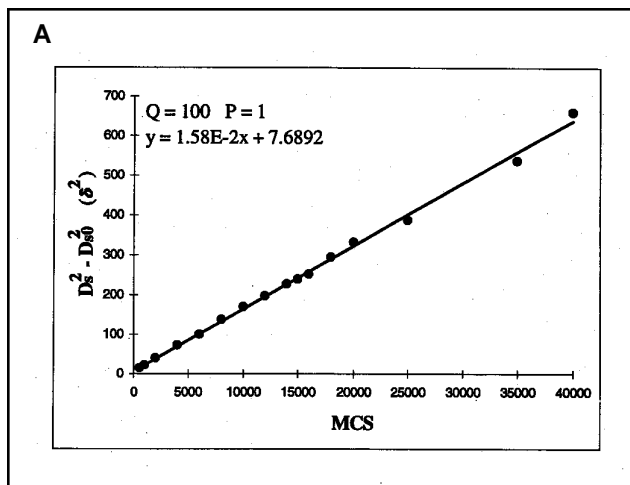


Fig. 4 — Results of isothermal simulations based on parabolic growth,  $n = 2$ , with different  $P_1$  values. A —  $P_1 = 1.0$ ; B —  $P_1 = 0.1$ .

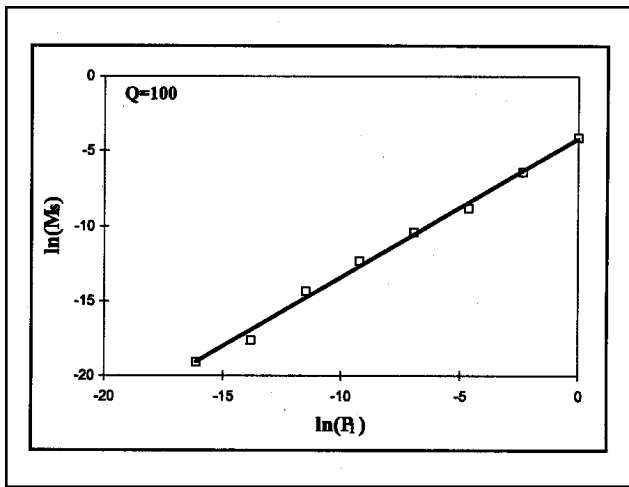


Fig. 5 — Results of isothermal simulations with various n values.

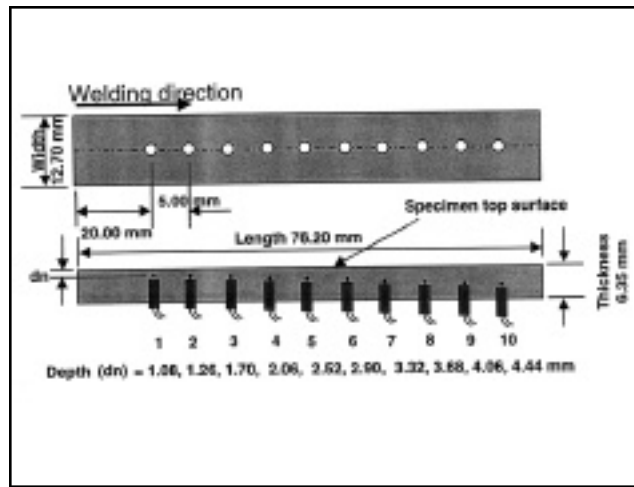


Fig. 6 — A laser welding specimen with ten holes drilled for mounting thermocouples.

2-mm region, a of 10 μm is selected to give a 200 x 200 matrix. Inserting into Equation 16b gives

$$MCS = \frac{K_s}{K_0} \frac{0.00001m^2}{1m} \text{ sec} \quad (17)$$

The grain growth coefficient  $K_0$  of nickel is  $1.36 \times 10^{-3} \text{ m}^2/\text{s}$  (Ref. 16). Substituting the values of  $K_0$  and  $K_s$  into Equation 17 gives the equivalent time for an MCS as  $1.11 \times 10^{-9} \text{ s}$ .

**Heat-Affected Zone Microstructure Simulation**

The material selected for the simulation was commercially pure nickel, Ni 270. The unit length used in the simulation was 10 μm, which implies a 2 x 2-mm parallelogram (200 x 200 elements) with a height of 1.732 mm as the simulation matrix. Temperature histories measured during welding were applied to the simulation for each MCS. The location of the second thermocouple (Fig. 6) corresponds to the top of the simulation matrix. Thus, the matrix contains thermocouples 2, 3, 4, 5, and 6. The corresponding temperature histories used in the simulation are shown in Fig. 7A. Figure 7B shows the temperature histories superimposed on each other. Assuming quasisteady-state welding conditions, the curves in Fig. 7B correspond to the temperature histories at depths of 1.26, 1.70, 2.06, 2.52, 2.90, and 3.32 mm.

The activation energy of grain growth  $E_A$  used in the simulation was 27.5 kcal/(mol<sup>o</sup>K) and the grain growth coefficient  $K_0$  was  $1.36 \times 10^{-3} \text{ m}^2/\text{s}$  (Ref. 16). The activation energy was selected to be the average of activation energies with grain orientation misfit angle from 20 to

80 deg, shown in Table 2.

The computation time required for a 200 x 200 matrix can be overwhelming. This is especially true with the normally low probability values obtained from Equation 11. To save computation time, a probability factor,  $P_{\text{factor}}$  is introduced for the simulations. The basic assumption is that the growth behavior for simulations at low probabilities is similar to that at high probabilities. From Equation 12, it is evident the growth behavior is governed by the  $K_s P_1 t_s$  term. A higher probability essentially reduces the time required to reach a particular grain size. The probability factor,  $P_{\text{factor}}$  is then defined as

$$P_{\text{factor}} = \frac{P_{1,\text{new}}}{P_{1,\text{old}}} \quad (18)$$

where  $P_{1,\text{new}}$  is the new probability, usually equal to 1, and  $P_{1,\text{old}}$  is the original probability given by Equation 11.

The probability factor for welding simulations is determined by setting the new probability for the point that experienced the highest temperature to 1. The peak temperature of the first curve in Fig. 7B is 1089.3°C (1362.3 K). Therefore, the maximum probability for this simulation,  $P_{1,\text{max}}$  is  $3.74 \times 10^{-5}$  and the  $P_{\text{factor}}$  for this simulation is the inverse of  $P_{1,\text{max}}$ , 26773.7, and thus reduces the simulation steps from  $4.80 \times 10^9$  to  $1.80 \times 10^5$ . Table 1 shows the parameters used in the simulation.

**Experiments**

**Specimen Preparation**

The material used in the experiment was originally hot-rolled (in the as-

received condition) nickel 270 (Ni 270), with purity 99.9% or greater, and was tempered in the laboratory at 600°C for 30 min to relieve any residual stresses that might have been produced during manufacturing. The tempered Ni 270 was then cold rolled from 13.72 to 6.86 mm with a 50% thickness reduction and was subsequently machined to 6.35-mm thickness, 12.70-mm width, and 76.20- mm length for laser beam welding. The specimen was first cut to approximate dimensions on a band saw and then milled to the final dimensions. Cutting fluids, water, and cutting oil for the band saw and mill, respectively, were used to minimize the impact of heat from material removal and to enhance the surface finish. Specimens for the normal grain growth investigation were then subjected to a recrystallization treatment, heated at 700°C for 30 min, to produce homogeneous grain size distribution in the material before laser beam welding.

Specimen surface conditions are important in laser beam welding. The specimens were, therefore, dry sanded using 400-grit silicon carbide paper to remove oxides and produce uniform scratches in the welding direction for a consistent surface condition. Ten blind holes were then drilled to different depths at different locations on the back of the specimen — Fig. 6. Each hole was initially drilled using a regular drill bit. The root of each hole was then flattened using a flat-headed drill bit. The actual depths were measured using a microscope after welding.

**Laser Beam Welding**

Autogeneous welding was done using a CO<sub>2</sub> laser at 1000-W power focused by a 125-mm (5-in.) focal length lens. The out-

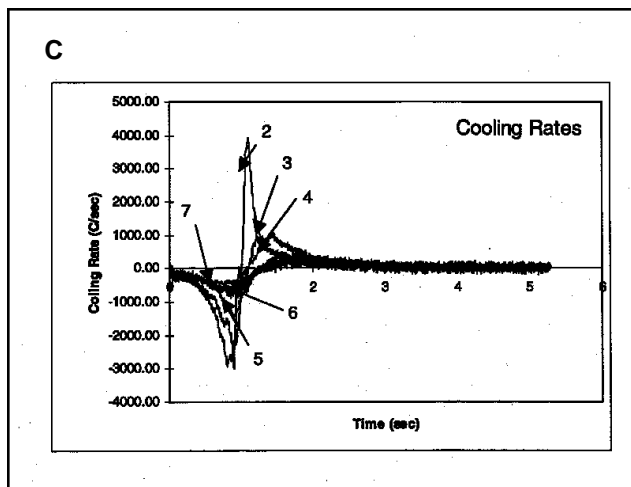
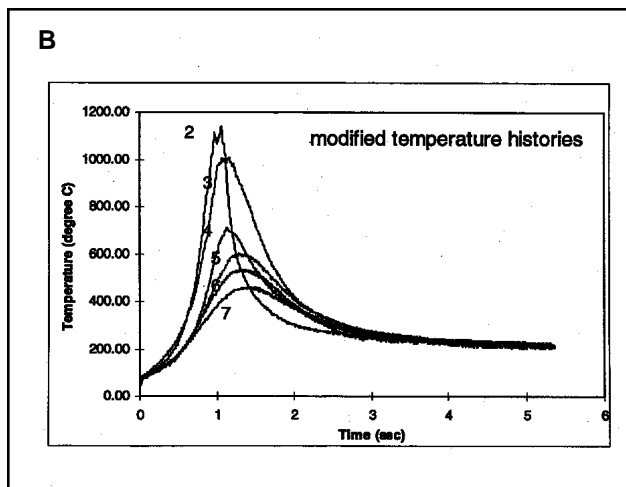
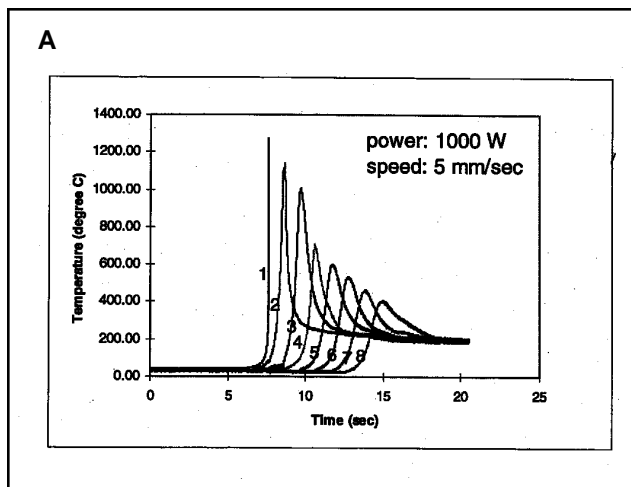


Fig. 7 — A — Temperature histories measured during laser welding; B — time-shifted temperature histories for grain growth simulation; C — cooling rates calculated from B.

put beam is D-mode [combined TEM<sub>00</sub> (60%) and TEM<sub>01</sub>\* (40%) modes], with a corresponding beam quality M<sup>2</sup> of about 2.0 (Ref. 17). The focal point was located on the specimen top surface with a diameter of about 250 μm and an incident angle of 3 deg. The welding speed was 5 mm/s. Argon was used as shielding gas at a flow rate of 21 L/min. To minimize heat conduction to the ambient, the specimen was supported by two ceramic tubes, each of 3.175 mm diameter.

**Temperature Measurement**

Temperature histories at various locations are necessary for dimensional grain growth simulations. K-type thermocouples (chromel-alumel) of 0.005 in diameter were used in the experiments. These were mounted in the plane along the welding direction, to measure temperatures vertically below the centerline of the

weld — Fig. 6. Bare thermocouple wires were protected by two-hole ceramic tubes, 1.5875-mm outer diameter and 0.3969-mm inner diameter, mounted into the predrilled holes on the back of the specimen. The thermocouples were welded to the flattened bottoms of the blind holes by capacitive discharge welding to firmly attach them to the specimen. Due to the guiding two-hole ceramic tubes, each thermocouple tip was centered very well, as observed after laser beam welding, microscopically. Each contact was carefully examined by measuring the electric resistance between the thermocouple and the specimen.

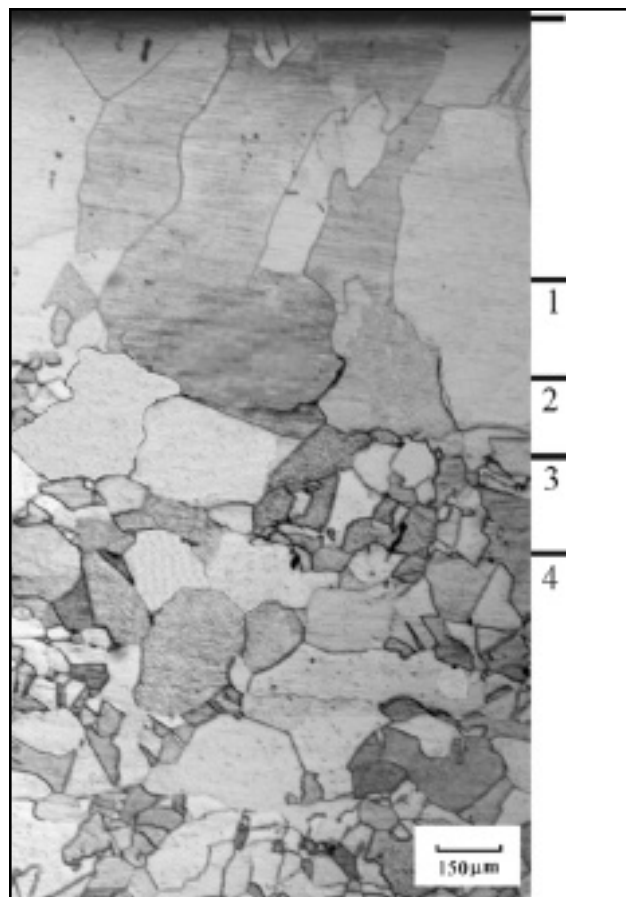


Fig. 8 — Microstructure of laser-beam-welded nickel in the plane under the weld and parallel to the welding direction.

A 486 PC with a 10-channel, 12-bit data acquisition system was used to record the temperature variations during welding. The channels were connected to the thermocouples at a selected sampling rate of 146.4 Hz per channel. A high sampling rate allowed more temperature data to be recorded during welding, en-

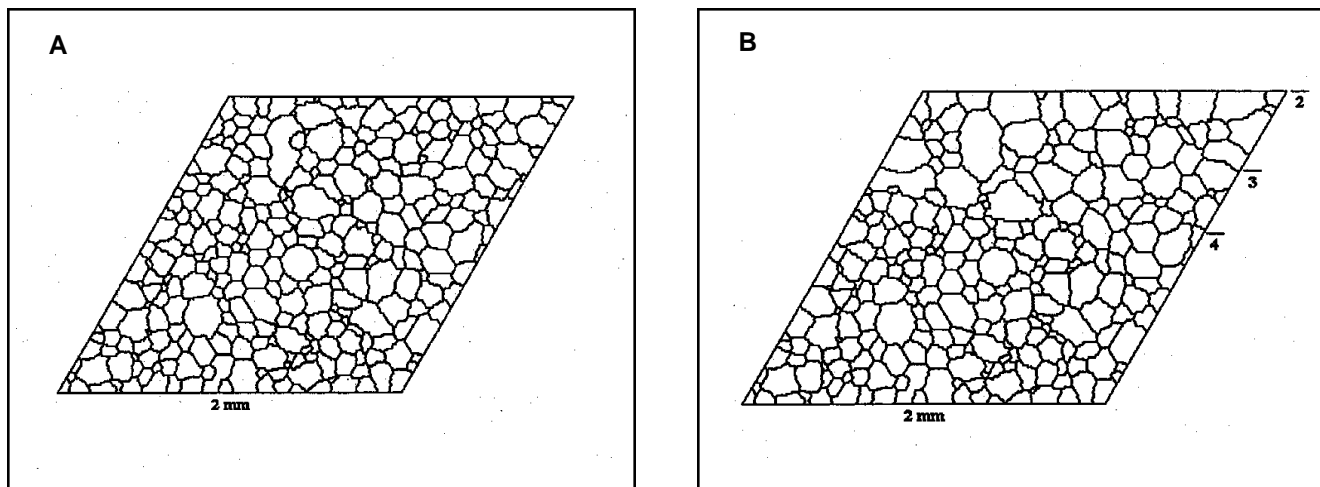


Fig. 9 — Monte Carlo simulation results of the heat-affected zone microstructure. A — Before welding; B — after welding.

abling smoother temperature histories. The temperature histories were then applied to the subsequent HAZ microstructure simulation.

## Results and Discussion

Due to the low heat input rate (1000 W), only conduction mode of fusion was observed in the weld. That is, no keyhole formation was obtained. Figure 7A shows the temperature histories at eight locations, channels one through eight. The discontinuity observed in the first channel was due to the fact the thermocouple mounted in that hole smelted during welding. Subsequent cross-sectional examination showed the actual depth of that thermocouple was 1.08 mm, and that was very close to the fusion zone, 0.98 mm deep. Figure 7B shows the modified temperature histories obtained by shifting each temperature history toward the second channel by an amount of time equal to its distance to the second channel divided by the welding speed. For example, channel 3 was shifted 1 second while channel 4 was shifted 2 seconds to the left. Under quasi-equilibrium welding conditions, it is assumed each point of the same depth, except those points near the ends of the specimen, experienced the same temperature history following a certain amount of time delay. Therefore, the curves in Fig. 7B relate to temperature histories at the locations of depths equal to 1.26, 1.70, 2.06, 2.52, 2.90, and 3.32 mm. These depths were determined after welding using a microscope at 100X magnification, to measure the cross-section of the sample along the center of the weld line. Temperatures at sites located between two thermocouples were approximated by linear interpolation for the Monte Carlo simulation. Cooling rates for

the temperature histories in Fig. 7B were calculated and are shown in Fig. 7C. Each data point in the cooling rate chart (Fig. 7C) was calculated by taking the average of 11 consecutive cooling rate data points, 5 before and 5 after the point of interest. From the cooling rate profiles, it was found channels 3 and 4 reached their peak temperatures at about the same time. This might have resulted from a small contact area between the joint nugget of the third thermocouple (channel 3) and the specimen. The actual contact area could not be measured.

Figure 8 shows an optical micrograph of the microstructure of the vertical cross-section located under the weld and parallel to the welding direction. The specimen was etched using an etchant containing 50% nitric acid and 50% glacial acetic acid. Locations 1, 2, 3, and 4 correspond to the locations of thermocouples 1, 2, 3, and 4, respectively. Average grain size at each location was measured by the Heyn lineal intercept method (Ref. 18) with at least 50 interceptions on an intercept line, using an optical microscope at a magnification of 100.

Each grain size value of the simulation results was taken as an average of five measurements around the location of interest. Figure 9A, simulated with a homogeneous temperature distribution

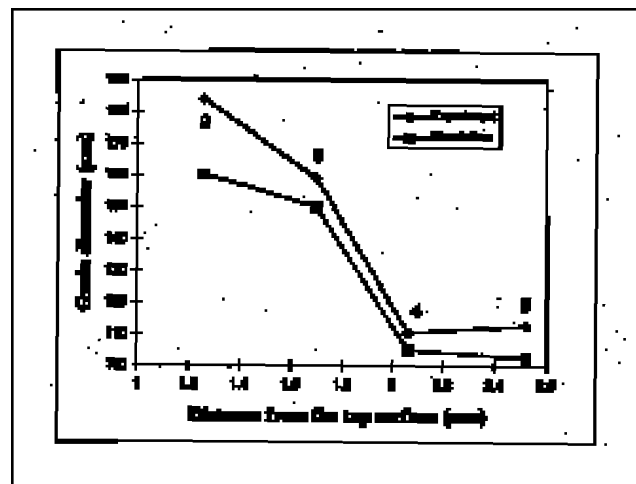


Fig. 10 — Grain size distributions from experiment and simulation.

starting with a randomly oriented matrix, illustrates a typical initial grain structure before welding, and Fig. 9B shows the heat-affected zone grain structure obtained by Monte Carlo simulation after welding. The location of the second thermocouple shown in Fig. 6 is the top of the simulation matrix shown in Fig. 9. Therefore, the matrix of the simulation contains thermocouples 2, 3, 4, 5, and 6. Temperatures at sites located between two thermocouples were approximated by linear interpolation. The average initial grain size of the material (obtained after the recrystallization treatment) was 113.1  $\mu\text{m}$ , taken from three measurements in the unaffected zone, while the average initial grain size obtained for the simulated microstructure was 111.2  $\mu\text{m}$ . The slight difference in the two average initial grain sizes is due to the fact that it was

very difficult getting the average grain size of the simulated microstructure to a specific value that would exactly match that of the actual material.

The simulated grain size distributions at channels 2, 3, 4, and 5 are shown in Fig. 10. Compared to the experimental results, the simulation errors in average grain size were 12.9%, 5.8%, 5.0%, and 9.2% at locations 1.26, 1.70, 2.06, and 2.52 mm below the weld centerline, respectively. The larger error of the simulation results at locations close to the fusion zone boundary is due to the missing of the peak temperature at the second channel. This resulted in a smaller total heat input to the corresponding location in the simulation. The second reason causing the deviation of the simulation results from experimental results was a slight difference in compositions for the materials used for the experiments and the simulations. The experimental material was a commercially pure nickel, Ni 270. However, due to the unavailability of all the data needed for this material, the activation energy  $E_A$  and grain growth coefficient  $K$  values used for the simulation were those of nickel bicrystals with a small amount of aluminum inside the crystals. Despite the slight difference in material properties, the results show reasonably good agreement on grain size prediction, with the simulation and experimental results following the same trend.

## Conclusions

Normal grain growth was assumed to be the major growth mechanism in the heat-affected zone during welding for a commercially pure annealed nickel. Compared to the experimental results,

the simulation errors in average grain size were 12.9 and 5.8% at locations 1.26 and 1.70 mm below the weld centerline, respectively. The trend of grain size distribution is similar in both experimental and simulation results.

Complete development of the grain growth simulation methodology will enable it to be applied to other manufacturing processes that involve high temperatures, such as heat treatment. This is provided the temperature history is either available or predictable and the grain growth properties (such as activation energy and grain growth coefficient) of the material are available.

## References

- Burke, F. E., and Turnbull, D. 1952. Recrystallization and grain growth. *Progress in Metal Physics* 3: 220–292.
- Feltham, P. 1957. Grain growth in metals. *Acta Metallurgica* 5(2): 97–105.
- Hillert, M. 1965. On the theory of normal and abnormal grain growth. *Acta Metallurgica*, 13(3): 227–238.
- Saetre, T. O., Hunderi, O., and Ryum, N. 1989. Modeling grain growth in two dimensions. *Acta Metallurgica* 37(5): 1381–1387.
- Hoffman, R. E., Pikus, F. W., and Ward, R. A. 1956. Self-diffusion in solid nickel. *Transactions AIME Journal of Metals*, pp. 483–486.
- Feltham, P., and Copley, G. J. 1958. Grain-growth in  $\alpha$ -Brasses. *Acta Metallurgica* 6: 539–542.
- Ghauri, I. M., Butt, M. Z., and Raza, S. M., 1990. Grain growth in copper and alpha-brasses. *Journal of Materials Science* 25: 4782–4784.
- Srivatsan, T. S. 1992. Microstructure, tensile properties and fracture behaviour of aluminium alloy 7150. *Journal of Materials Science* 27: 4772–4781.
- Srolovitz, D. J., Anderson, M. P., and Sahni, P. S. 1984. Computer simulation of grain growth — II: Grain size distribution, topology, and local dynamics. *Acta Metallurgica* 32(5): 793–802.
- Anderson, M. P., Srolovitz, D. J., Grest, G. S., and Sahni, P. S. 1984. Computer simulation of grain growth — I: Kinetics. *Acta Metallurgica* 32(5) 783–791.
- Gao, J., and Thompson, R. G. 1996. Real time-temperature models for Monte Carlo simulations of normal grain growth. *Acta Metallurgica* 44: 4565–4570.
- Radhakrishnan, B., and Zacharia, T. 1995. Monte Carlo simulation of grain boundary pinning in the weld heat affected zone. *Metallurgical and Materials Transactions A* 26A: 2123–2130.
- Li, M. Y., and Kannatey-Asibu, Jr., E. 1994. Computational heat-affected zone microstructure simulation — normal grain growth. *Proceedings of the Laser Materials Processing Conference, ICALEO '94*, 79: 658–667.
- Metzbower, E. A., and Moon, D. W. 1985. Laser beam welding of ASTM A-36 steel. *Proceedings Lasers in Metallurgy*, 110th AIME Annual Meeting, Chicago, Ill., pp. 255–262.
- Metzbower, E. A. 1990. Laser beam welding: Thermal profiles and HAZ hardness. *Welding Journal* 69(7): 272-s to 278-s.
- Upthegrove, W. R. 1956. Grain boundary and lattice self-diffusion of nickel. Doctoral dissertation, The University of Michigan, pp. 128–132.
- PRC Corp., manufacturer's specification, PRC, Landing, N.J.
- ASTM. 1983. Annual Book of ASTM — Standards Metals Test Methods and Analytical Procedures. ASTM, 3.3: 121–155.